Phonon-assisted indirect transitions in angle-resolved photoemission spectra of graphite and graphene

Pourya Ayria,[1,*] Shin-ichiro Tanaka,[2] Ahmad R. T. Nugraha,[1] Mildred S. Dresselhaus,[3,4] and Riichiro Saito[1]

[1]*Department of Physics, Tohoku University, Sendai 980-8578, Japan*
[2]*The Institute of Scientific and Industrial Research, Osaka University, Osaka 567-0047, Japan*
[3]*Department of Electrical Engineering, Massachusetts Institute of Technology, Cambridge, Massachusetts 02139-4307, USA*
[4]*Department of Physics, Massachusetts Institute of Technology, Cambridge, Massachusetts 02139-4307, USA*

Indirect transitions of electrons in graphene and graphite are investigated by means of angle-resolved photoemission spectroscopy (ARPES) with several different incident photon energies and light polarizations. The theoretical calculations of the indirect transition for graphene and for a single crystal of graphite are compared with the experimental measurements for highly-oriented pyrolytic graphite and a single crystal of graphite. The dispersion relations for the transverse optical (TO) and the out-of-plane longitudinal acoustic (ZA) phonon modes of graphite and the TO phonon mode of graphene can be extracted from the inelastic ARPES intensity. We find that the TO phonon mode for **k** points along the Γ-K and K-M-K' directions in the Brillouin zone can be observed in the ARPES spectra of graphite and graphene by using a photon energy ≈ 11.1 eV. The relevant mechanism in the ARPES process for this case is the resonant indirect transition. On the other hand, the ZA phonon mode of graphite can be observed by using a photon energy ≈ 6.3 eV through a nonresonant indirect transition, while the ZA phonon mode of graphene within the same mechanism should not be observed.

I. INTRODUCTION

Angle-resolved photoemission spectroscopy (ARPES) is one of the well-known methods to probe the electron-phonon interaction in solids [1]. Renormalization of the electronic energy due to the electron-phonon interaction has been explored by the observation of the electron dispersion relation near the Dirac point (the K or K' points of the hexagonal Brillouin zone) in graphene [2–4]. The electron-phonon renormalization causes the appearance of a kink structure in the electron dispersion relation. The ARPES intensity is expressed in terms of the self-energy, in which the real and imaginary parts of the self-energy determine the kink structure and the linewidth in the electronic energy dispersion relations, respectively [5,6].

It is known that the ARPES spectra around the Γ point and near the Fermi level (with binding energies around $E_b \approx$ 0–3 eV) do not exist for the direct optical transition because there is no corresponding energy state [2]. However, recent ARPES experiments show that measurement of the ARPES intensity around the Γ point and near the Fermi level could also provide valuable information on the electron-phonon interaction [7,8]. For example, Liu *et al.* have observed the ARPES spectra at the Γ point and near the Fermi level for graphene-based materials [7]. They pointed out that the observation of ARPES spectra originates from the *indirect transition* of electrons, which is mediated by phonons. In their experiment, the observed ARPES spectra with binding energies around 154 meV and 67 meV have been ascribed to the energy and momentum of the phonon at the K (or K') point. They suggest that the electron is scattered from the K to the Γ point by emitting a phonon through an indirect transition. However, the phonon dispersion from their experiment could

not be determined because they used photon energies of more than 20 eV.

Tanaka *et al.* have reported ARPES spectra of highly-oriented pyrolytic graphite (HOPG) around the Γ point and near the Fermi level for various photon energies less than 15 eV [8]. This experiment probes the energies and momenta of the electrons and phonons involved in the indirect transition, for different photon energies, so that the phonon dispersion of HOPG can be obtained. They found that, when the incident p-polarized photons are incident on the sample surface, the ARPES intensity increases like a step function at the binding energies around 154 meV and 67 meV for $\hbar\omega = 11.1$ eV and for $\hbar\omega = 6.3$ eV, respectively, and that the ARPES spectra cannot be observed for incident photons in the range $\hbar\omega =$ 13–15 eV in their experiment. However, not all the possible phonon dispersion relations of graphite could be well resolved since HOPG is not a single crystal of graphite. Thus, the phonon modes involved in the indirect transition were not assigned properly from previous experimental measurements which were based on HOPG.

In this paper, motivated by the observations of the indirect transition ARPES spectra [7,8], we investigate the detailed mechanisms of indirect transitions in graphene and graphite by the calculation of the electron-photon interaction and the electron-phonon interaction based on first principles calculations [9–12]. By considering the indirect transition, we compare our theoretical calculation of the ARPES intensity with the latest data from experimental measurements for HOPG and a single crystal of graphite in order to evaluate and assign the origin of the observation of the phonon dispersion in graphene and graphite through ARPES for various photon energies. We find that the dispersion relations of the transverse optical (TO) and of the out-of-plane acoustic (ZA) phonon modes of graphene and graphite which have even symmetry with respect to a mirror plane (i.e., a plane which includes the incident light and the ejected photoemission electron)

_____

*pourya@flex.phys.tohoku.ac.jp

can be extracted from the experimental ARPES intensity. Although the longitudinal acoustic (LA) phonon mode also has even symmetry with respect to the mirror plane, the LA phonon mode cannot be observed due to the negligibly small electron-phonon matrix element in the vicinity of the K point.

We also find that the ARPES spectra near the binding energy of 154 meV can be assigned by the ARPES intensity calculation as the TO phonon mode for the applied photon energy $\hbar\omega \approx 11.1$ eV, in which the relevant mechanism involves the resonant indirect transition. On the other hand, for the lower photon energy $\hbar\omega \approx 6.3$ eV, the ZA phonon mode is assigned to the ARPES spectra at the binding energy of 67 meV through the nonresonant indirect transition with p-polarized light. In the case of the photon energy $\hbar\omega = 13$–15 eV, we will show that the ARPES intensity cannot be observed because the directions of the ejected electron and the detector are not properly aligned with respect to each other to have a significant ARPES intensity.

This paper is organized as follows. In Sec. II we describe the geometry of the ARPES measurements, the experimental setup, and the theoretical formulation of the indirect transition. We also discuss the symmetry considerations for the ARPES spectra by group theory. In Sec. III, theoretical results for the ARPES spectra are compared with the experimental measurements. Finally, the summary of this paper is given in Sec. IV.

II. METHODS

A. ARPES experiments

In Fig. 1, the experimental setup is shown schematically, in which the graphene surface is irradiated by photons having an incident angle ψ with respect to the z axis, normal to the surface. The emitted electrons with an emission angle θ are analyzed with respect to the kinetic energy and momentum [13].
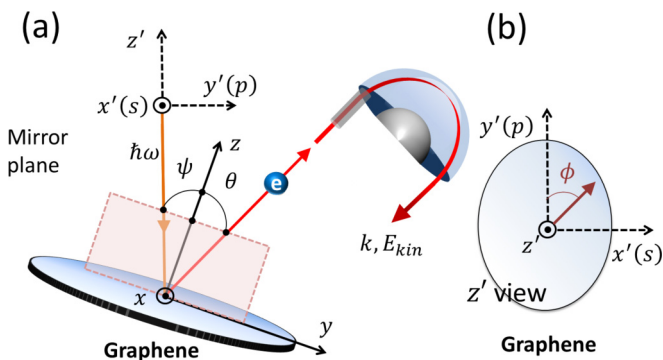

FIG. 1. (a) Geometry of the photoemission process [9]. The incident photon with energy $\hbar\omega$ is shown by an arrow going to the graphene plane. We can define a mirror plane which contains the directions of the incident light (z' axis), the electrons ejected from the surface, and an axis (z axis) normal to the graphene surface. The angles between the incident light, the ejected electron, and the z axis are denoted by ψ, θ, respectively. (b) Viewing the setup from the z' axis, the light polarization angle ϕ is in the $x'y'$ plane and is measured with respect to the y' axis. Here, $\phi = 0°$ and $\phi = 90°$ correspond to the p and s polarizations, respectively.

When we look at the surface in the direction of the z' axis, we see that the light polarization angle ϕ is defined in the $x'y'$ plane and measured by the y' axis, as shown in Fig. 1(b). Here, $\phi = 0°$ and $\phi = 90°$ correspond to the p- and s-polarization directions, respectively [9,14–16]. In this paper, we adopt a particular geometry so that the analyzer is perpendicular to the surface, i.e., $\theta = 0$. The experiments were carried out at two beamlines of the synchrotron radiation facilities: (1) the BL-7U facility of UVSOR at the Institute for Molecular Science, Okazaki, Japan and (2) the BL-9A facility of HiSOR at Hiroshima University, Higashi-Hiroshima, Japan. The photon energy dependence of the HOPG was taken at the BL-7U facility and the polarization dependence of the single-crystalline graphite was taken at the BL-9A facility. In both beamlines, the combination of the APPLE-II-type variable-polarization undulator, normal incidence monochromator, photoelectron spectrometer with a multichannel detector, and a precise multiaxis goniomer for the sample enables us to measure the ARPES spectra with sufficient resolution for observing the phonons (< 10 meV). The sample was kept at 30 K during the measurement with a He cryostat.

B. Formulation of ARPES intensity

Let us define the Hamiltonian; H_e for electrons, H_{ph} for phonons, H_{opt} for the electron-photon interaction, and H_{ep} for the electron-phonon interaction. The total Hamiltonian H is written as

$$H = H_e + H_p + H_{\mathrm{opt}} + H_{\mathrm{ep}}, \tag{1}$$

where the unperturbed Hamiltonian of electrons and phonons is considered as $H_0 = H_e + H_p$. We adopt the adiabatic approximation, which implies that the total wave function can be written as a product of an electron eigenstate and phonon eigenstate [6].

The unperturbed electron and phonon dispersion relations and their eigenstates for points along the high symmetry axes are calculated using the QUANTUM ESPRESSO package [12]. For the electron calculation, we adopt the norm-conserving pseudopotential with the Perdew-Zunger exchange-correlation scalar relativistic functional. The kinetic energy cutoff is taken as 60 Ry for each atom and the kinetic energy cutoff for the electron density potential is set to be 600 Ry in order to verify the convergence of all wave functions. The k points for the self-consistent calculation are taken within the $42 \times 42 \times 1$ and $20 \times 20 \times 4$ mesh grids in the graphene and graphite Brillouin zones, respectively. The lattice parameter of graphene is considered to be 2.46 Å and the lattice constant in the direction normal to the graphene plane is taken as $c/a = 20.0$ and $c/a = 2.7$ for graphene and graphite, respectively. As for the phonon calculation, we adopt the Perdew-Burke-Ernzerhof generalized gradient approximation for the exchange-correlation function [17]. The kinetic energy cutoff is set to be 100 Ry for each atom, while the kinetic energy cutoff for the density potential is taken as 1200 Ry. Following Ref. [18], the dynamical matrix is calculated on $6 \times 6 \times 1$ and $6 \times 6 \times 4$ q-point mesh grids in graphene and graphite, respectively, where q is the phonon wave vector.

The calculated electron energy dispersions of graphite and graphene are shown in Figs. 2(a) and 2(b), respectively,
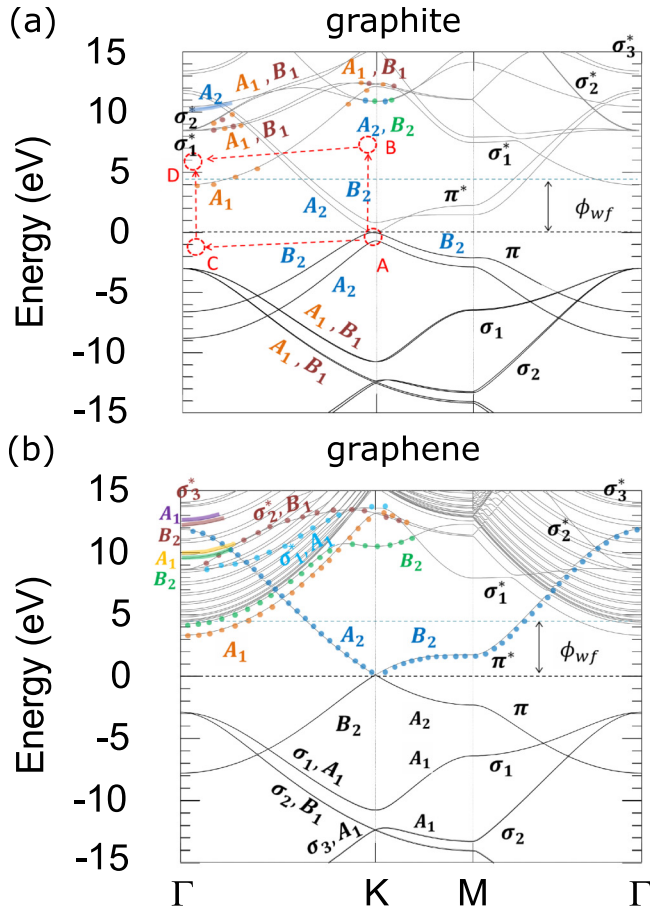
FIG. 2. Electronic energy dispersion relations of (a) graphite and (b) graphene are calculated by first-principles calculations and plotted along the high symmetry directions Γ-K-M-Γ up to 15 eV. In panel (a), the two possibilities of indirect transitions ($A \to B \to D$ and $A \to C \to D$) are shown by the red dash-dotted arrows, in which an electron from the initial state A can reach the final state D mediated by electron-phonon interaction. The separation between the states A and B (or C and D) is determined by the incident photon energy used in ARPES (in this picture it is $\sim$7 eV). Note that in both panels (a) and (b) we show some symmetry representations for the energy bands which might be involved in the indirect transitions in (a) graphite and (b) graphene.
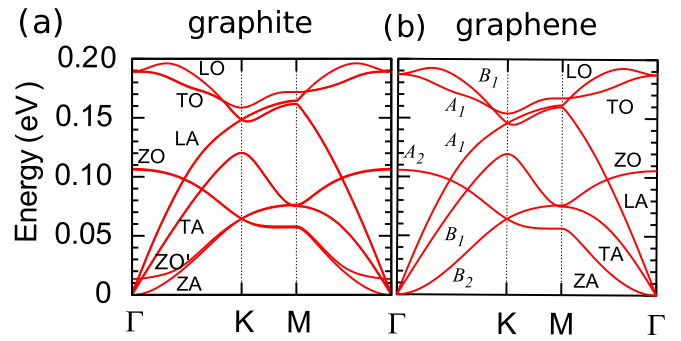

FIG. 3. The phonon energy dispersion relations for (a) graphite and (b) graphene, obtained from first-principles calculations and density functional perturbation theory [12]. Since there is C_{2v} symmetry along the Γ-K-M and Γ-M directions, each phonon mode is labeled by the irreducible representation of the C_{2v} point group along the Γ-K-M direction [19]. The TA, LA, TO, and LO phonon modes along Γ-K-M correspond to B_1, A_1, A_1, and B_1 symmetries, respectively. The ZA and ZO phonon modes along the Γ-K-M correspond to B_2 and A_2 symmetries.

the out-of-plane optical phonon mode, which are labeled as TO, LO, and ZO, respectively. The symmetry labels of the phonon modes of graphene are also shown in Fig. 3(b) which will be discussed in the next section.

The perturbation Hamiltonian in Eq. (1) is considered as

$$H' = H_{\text{opt}} + H_{\text{ep}}. \tag{2}$$

The transition rate from an initial state $|i\rangle$ to a final state $|f\rangle$ through a virtual state $|m\rangle$ is given by the second-order time-dependent perturbation theory [10,11],

$$W(\mathbf{k}_f, \mathbf{k}_i) = \frac{2\pi}{\hbar} |S(\mathbf{k}_f, \mathbf{k}_i)|^2 \delta(\varepsilon_i - \varepsilon_f), \tag{3}$$

where ε_i and ε_f represent the energy of an initial state and a final state, respectively, and the matrix $S(\mathbf{k}_f, \mathbf{k}_i)$ is given by

$$S(\mathbf{k}_f, \mathbf{k}_i) = \sum_m \frac{\langle f|H'|m\rangle \langle m|H'|i\rangle}{\varepsilon_i - \varepsilon_m}. \tag{4}$$

There are two scattering processes following Eq. (4) that may contribute to the indirect transition, i.e., $A \to B \to D$ and $A \to C \to D$, which are depicted as red dash-dotted arrows in Fig. 2(a). In the $A \to B \to D$ process: (1) a photon excites an electron from the initial state $|A\mathbf{k}_i\rangle$ to a state $|B\mathbf{k}_m\rangle$ and then (2) the photoexcited electron from the state $|B\mathbf{k}_m\rangle$ is scattered to the final state $|D\mathbf{k}_f\rangle$ by emitting a phonon. Since the temperature of the sample is considered to be 60 K, the probability absorption of a phonon in the $A \to B \to D$ process is negligible. In the $A \to C \to D$ process: (1) a phonon scatters an electron from the initial state $|A\mathbf{k}_i\rangle$ to a state $|C\mathbf{k}_m\rangle$ and then (2) a photon excites the scattered electron from the state $|C\mathbf{k}_m\rangle$ to the final state $|D\mathbf{k}_f\rangle$. All these processes are expressed by the following equation:

$$S(\mathbf{k}_f, \mathbf{k}_i) = \frac{\langle D\mathbf{k}_f, |H_{\text{ep}}|B\mathbf{k}_m\rangle \langle B\mathbf{k}_m|H_{\text{opt}}|A\mathbf{k}_i\rangle}{E_i(\mathbf{k}_i) + \hbar\omega - E_B(\mathbf{k}_i)}$$
$$+ \frac{\langle D\mathbf{k}_f|H_{\text{opt}}|C\mathbf{k}_m\rangle \langle C\mathbf{k}_m|H_{\text{ep}}|A\mathbf{k}_i\rangle}{E_i(\mathbf{k}_i) - \hbar\omega_q^\alpha - E_C(\mathbf{k}_f)}, \tag{5}$$

whereas the calculated phonon dispersion of graphite and graphene are shown in Figs. 3(a) and 3(b), respectively. Since there are four atoms in the unit cell of graphite, there will be twelve phonon modes. Most of the phonon modes are nearly doubly degenerate and similar to those for graphene [20,21]. Thus, we put the same labels of phonon modes for graphite and graphene, except for the breathing mode (ZO$'$) of two layers in graphite. In graphene, there are six phonon modes which consist of four in-plane modes and two out-of-plane modes. At the Γ point, there are three acoustic branches: (1) the transverse acoustic, (2) the longitudinal acoustic, and (3) the out-of-plane acoustic phonon modes, which are labeled in Fig. 3(b) as TA, LA, and ZA, respectively. Unlike the case of graphite, there is no ZO$'$ mode in graphene. There are also three optical phonon modes in graphene above 0.1 eV at the Γ point: (1) the transverse optical, (2) the longitudinal optical, and (3)

where the energy and momentum conservation requirement gives the energy denominators of Eq. (5) and $\mathbf{k}_f = \mathbf{k}_i + \mathbf{q}$. In Eq. (5), $\hbar\omega$ denotes the photon energy and $\hbar\omega_q^\alpha$ refers to the energy of the αth phonon mode with the wave vector $\mathbf{q}$. After calculations, we find that the $A \to B \to D$ transition would be more dominant than the $A \to C \to D$ transition both for photon energies around $\hbar\omega \approx 11$ eV–15 eV and for lower photon energies around $\hbar\omega \approx 6$ eV. However, it should be noted that there are different physical origins for why the $A \to B \to D$ transition is always dominant in the two different energy ranges, as will be discussed in Sec. III.

We adopt the rigid-ion approximation for the electron-phonon matrix element $\langle f, \mathbf{k}_f | H_{\mathrm{ep}} | i, \mathbf{k}_i \rangle$ [6,22], whose detailed derivation is given in Appendix A. In the case of the electron-photon transition from an initial state $|i, \mathbf{k}\rangle$ to a final state $|f, \mathbf{k}\rangle$, the electron-photon matrix element is given in the dipole approximation [23], while $\langle f, \mathbf{k} | H_{\mathrm{opt}} | i, \mathbf{k} \rangle \propto \mathbf{A} \cdot \mathbf{D}(\mathbf{k})$, where $\mathbf{A}$ is the vector potential and $\mathbf{D}(\mathbf{k}) = \langle f, \mathbf{k} | \nabla | i, \mathbf{k} \rangle$ is the dipole vector. The electron-photon interaction for different photon energies based on the plane wave expansion is discussed in the previous study [9], and we follow the same method in the present work to calculate the electron-photon matrix element.

To obtain the ARPES intensity $I(E, \hbar\omega)$, we need to integrate over all the initial states and all the final states. The summation on the initial states and the final states can be performed independently when we adopt the experimental conditions that are chosen for each ARPES experiment [24]. The ARPES intensity $I(E, \hbar\omega)$ is given by

$$I(E, \hbar\omega) \propto \sum_{i,f} \int d\mathbf{k}_i d\mathbf{k}_f |S(\mathbf{k}_f, \mathbf{k}_i)|^2 \delta(\varepsilon_i - \varepsilon_f)$$
$$\times \delta(E - \varepsilon_f + \phi_{\mathrm{wf}})(N_q^\alpha + 1) f_F^{\mathrm{occ}}, \quad (6)$$

where $\phi_{\mathrm{wf}} = 4.5$ eV is the work function of graphene [25], f_F^{occ} denotes the Fermi-Dirac distribution function for the occupied state and N_q^α is the quantum number of the phonon mode α with wave vector $\mathbf{q}$. The first delta function in Eq. (6) expresses conservation of total energy, while the second delta function ensures that the photoelectrons have higher energies than the work function ϕ_{wf}. In addition, there are several symmetry selection rules for the ARPES spectra in graphite and graphene, especially for the indirect transition. These selection rules are discussed in the next section.

C. Symmetry selection rules for ARPES

The geometry of the indirect scattering of electrons is schematically illustrated in Fig. 4. The electrons around the K or K' point can scatter to the region near the Γ point by an indirect transition. The shaded region along the Γ-K direction displays the locations where the photoemitted electrons are measured in the ARPES experiment. The measurement of the ARPES intensity along the Γ-K line provides information about the phonon dispersion along Γ-K' and K-M-K' [7], which is explained in Appendix B.

In graphene and graphite, the three high-symmetry points Γ, K (or K'), and M correspond to the D_{6h}, D_{3h}, and D_{2h} point group symmetries, respectively. The electronic states along the K'-Γ-K and K'-M-K lines belong to the C_{2v}
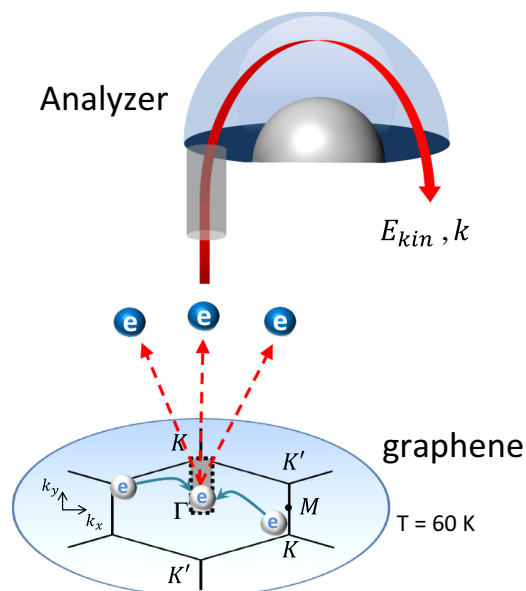

FIG. 4. The indirect scattering of an electron. An electron around the K or K' point scatters around the Γ point by the indirect transition. The shaded region line along Γ-K is what we observed for E_{kin} and $\mathbf{k}$.

point group, while any other general $\mathbf{k}$ points belong to the C_{1h} point group [26–28]. The C_{2v} group has four irreducible representations $\{A_1, A_2, B_1, B_2\}$ as shown in Table I. According to the x, y, z coordinates in Fig. 4, the character table of C_{2v} is listed in Table I. Moreover, in the C_{2v} symmetry, there are two mirror plane operations $\sigma_v(xz)$ and $\sigma_v'(yz)$ in the Brillouin zone. The plane $\sigma_v(xz)$ is aligned with the M-Γ-M line, while the plane $\sigma_v'(yz)$ is aligned with the K-Γ-K' line. Since we observe ARPES spectra in the present study, along the K-Γ lines, $\sigma_v'(yz)$ is relevant to the ARPES spectra as shown below. As we explained, the symmetry labels of each of the phonon modes of graphene along the Γ-K-M lines are shown in Fig. 3(b).

The selection rules for the optical and lattice vibrations impose nonzero matrix elements $\langle m|o|i \rangle$ and $\langle f|q|m \rangle$ in Eq. (5), which satisfy [29]:

$$\Gamma_m \otimes \Gamma_o \otimes \Gamma_i = A_1 \quad \text{and} \quad \Gamma_f \otimes \Gamma_q \otimes \Gamma_m = A_1 \quad (7)$$

where Γ_i, Γ_m, Γ_f, Γ_o, Γ_q are, respectively, the irreducible representations for the initial state, intermediate state, and final state of the electron wave functions, the dipole vector, and the phonon mode.

Further, in the ARPES experiment, we need also to consider the conservation of parity for the matrix elements of the

TABLE I. Character table of the $C_{2v}(2mm)$ point group.

	E	C_2	$\sigma_v(xz)$	$\sigma_v'(yz)$	Bases
A_1	1	1	1	1	z, ∇_z
A_2	1	1	-1	-1	R_z
B_1	1	-1	1	-1	x, R_y, ∇_x
B_2	1	-1	-1	1	y, R_x, ∇_y

TABLE II. Direct product table of the C_{2v} representation for the indirect transition $A \to B \to D$. Here Γ_i indicates the initial states, $\Gamma_i = \{A_2, B_2\}$, while $\Gamma_o = \{A_1, B_1, B_2\}$ refers to the optical transition and Γ_q assigns the phonon eigenvector symmetry along Γ-K-M. For the final states $\Gamma_f = \{A_1, B_2\}$, the corresponding column shows the symmetry of the allowed final state.

Γ_i	Γ_o(Pol.)	Γ_m	Γ_m	Γ_q(Ph.)	Γ_f
B_2	$A_1(p)$	B_2	B_2	A_1(TO,LA)	B_2
B_2	$B_2(p)$	A_1	A_1	A_1(TO,LA)	A_1
B_2	$A_1(p)$	B_2	B_2	B_2(ZA)	A_1
B_2	$B_2(p)$	A_1	A_1	B_2(ZA)	B_2
A_2	$B_1(s)$	B_2	B_2	A_1(TO,LA)	B_2
A_2	$B_1(s)$	B_2	B_2	B_2(ZA)	A_1

product $\langle f|H'|m\rangle\langle m|H'|i\rangle$, in Eq. (4), under reflection from the mirror plane $\sigma'_v(yz)$ [13]. This condition imposes an additional restriction to get a nonzero ARPES intensity, i.e., the integral of $\langle f|H'|m\rangle\langle m|H'|i\rangle$ must be an even function for the $\sigma'_v(yz)$ symmetry operation. Furthermore, it is known that the final state $\langle f|$ must have even symmetry with respect to the mirror plane $\sigma'_v(yz)$ in the ARPES experiment [1,13,15,30].

If we consider the π band as the initial state Γ_i, this state has to have B_2 and A_2 symmetry, as shown in Fig. 2,

$$\Gamma_i = A_2 \quad \text{or} \quad B_2.$$

Since the final state Γ_f has to have even symmetry with respect to the mirror plane $\sigma'_v(yz)$, the final state belongs to the A_1 or B_2 irreducible representation,

$$\Gamma_f = A_1 \quad \text{or} \quad B_2.$$

Since most of the phonon branches of graphite are nearly doubly degenerate and almost similar to those in graphene, in the following symmetry discussion, we will use the symmetry of the phonons in graphene for simplicity [21]. Graphene has six phonon modes, as shown in Fig. 3(b). The four in-plane phonon modes TA, LA, TO, and LO along Γ-K-M transform as B_1, A_1, A_1, and B_1, respectively. The out-of-plane phonon modes ZA and ZO along Γ-K-M transform as B_2 and A_2, respectively [21,31,32]. Moreover, the parity under the $\sigma'_v(yz)$ reflection along the Γ-K line is odd for TA, LO, and ZO and is even for ZA, LA, and TO [33]. Thus, only the ZA, LA, and TO phonon modes can be observed in the ARPES spectra. It is important to note that the p-polarized light lies in the yz plane, shown in Fig. 1, and it transforms as the B_2, A_1 irreducible representations. The s-polarized light is parallel to the x axis and it transforms as the B_1 irreducible representation. In order to satisfy Eq. (4) there are six possibilities in the ARPES processes for $\langle m|o|i\rangle$ and $\langle f|q|m\rangle$, which are summarized in Table II.

III. RESULTS AND DISCUSSION

To investigate the observation of the ARPES spectra at the Γ point and near the Fermi level energy, we calculate here the indirect transition ARPES intensity as a function of the binding energy, for the **k** vectors very close to the Γ point, at $\mathbf{k} = 2\pi/a \times 10^{-4}$, along Γ-K for several photon energies of graphene

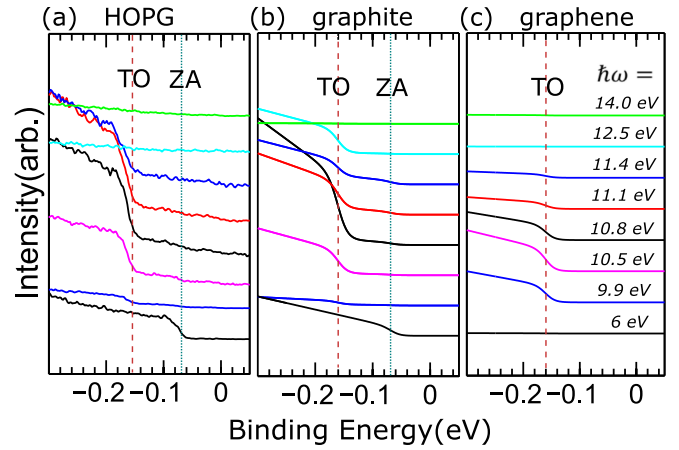
FIG. 5. (a) The experimental ARPES intensities for HOPG compared with the calculated ARPES intensities for (b) graphite and (c) graphene near the Γ point for several incident photon energies. The incident photon is p-polarized light and the incident angle is $\psi = 40°$. In (a), steplike features are found at the binding energy $E_b \approx 154$ meV (dashed line) and $E_b \approx 67$ meV (dotted line), which are assigned to the TO and ZA modes, respectively. In (b), the steplike features from the calculations for the TO and ZA modes are found to be at $E_b \approx 160$ meV and $E_b \approx 67$ meV, respectively. In (c), from our calculation, we find only the TO mode, but no ZA mode.

and graphite. Here, we consider the p-polarized light with an incident angle $\psi = 40°$ that is the same as the experimental setup. The calculated results can then be compared with the experimental ARPES spectra.

Figure 5(a) shows the experimental ARPES intensity as a function of the binding energy for highly-oriented pyrolytic graphite (HOPG), whereas Figs. 5(b) and 5(c) show the calculated ARPES intensity for graphite and graphene, respectively. Looking at Figs. 5(a) and 5(b), the calculated ARPES intensity basically reproduces the experimental data. We can see that there are steplike features in the ARPES intensity at the binding energies $E_b \approx 154$ meV and $E_b \approx 67$ meV for the experimental measurements and at $E_b \approx 160$ meV and $E_b \approx 67$ meV for the corresponding theoretical calculations for graphite. The small discrepancy between the experiment and theory for the positions of the steplike features might originate from the Kohn anomaly [5], which is neglected in our calculations for simplicity. We assign the steplike features at $E_b \approx 154$ meV (or 160 meV) and at $E_b \approx 67$ meV to the TO and ZA modes, respectively. Furthermore, in Fig. 5(c), we can see the steplike features only at $E_b \approx 160$ meV and there is no such feature at $E_b \approx 67$ meV. In the present work, we only perform the calculations for graphite and monolayer graphene. However, for the TO mode, we expect that the ARPES intensity in the case of few-layer graphene might show similar results to that of graphite. As for the ZA mode, few-layer graphene might show a transition from the feature of monolayer graphene to graphite. We will understand all these behaviors by discussing the detailed scattering processes in the following subsections.

A. Resonant indirect transitions

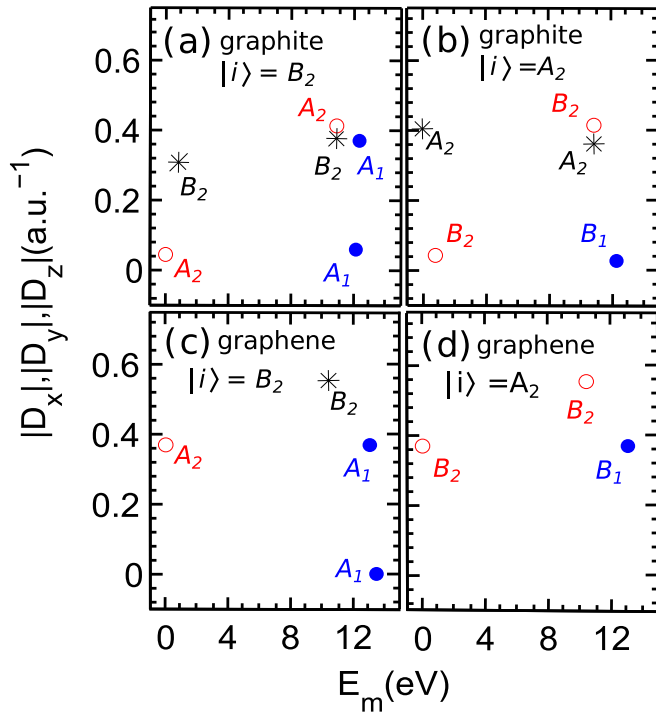For the photon energy range of 10–15 eV, it is possible to obtain a resonance process, and thus the ARPES intensity

FIG. 6. The x, y, and z components of the dipole vector, i.e., D_x (circles), D_y (full circles), D_z (asterisks), plotted as a function of the energy of the intermediate state (E_m) for (a) graphite with B_2 symmetry as the initial state, (b) graphite with A_2 symmetry as the initial state, (c) graphene with B_2 symmetry as the initial state, and (d) graphene with A_2 symmetry as the initial state. Symmetry labels near the circles, dots, and asterisks correspond to the symmetry of the intermediate states.

for the $A \rightarrow B \rightarrow D$ transition [see again Fig. 2(a)] is 10 times larger than that for the $A \rightarrow C \rightarrow D$ transition. In this case, the first step of the $A \rightarrow B \rightarrow D$ transition is the direct optical transition, $A \rightarrow B$, from the carbon π band to the conduction bands around the K point. For this purpose, in Fig. 6, we show the absolute value of the dipole vector, $\mathbf{D}(\mathbf{k}) = \langle m\mathbf{k}|\nabla|i\mathbf{k}\rangle$, as a function of the intermediate state energy for different conduction bands in graphite [Figs. 6(a) and 6(b)] and graphene [Figs. 6(c) and 6(d)]. For the initial states that satisfy Table II, we plot the dipole vectors for $|i\rangle = B_2$ [Figs. 6(a) and 6(c)] and for $|i\rangle = A_2$ [Figs. 6(b) and 6(d)]. The wave vector of the initial state of the electron is considered at a point with a distance of $2\pi/a \times 10^{-4}$ from the K point along the Γ-K line. The full circles, dots, and asterisks denote the x, y, and z components of the dipole vectors, i.e., D_x, D_y, and D_z, respectively. The symmetry of each intermediate state is also labeled.

More detailed information about the dipole vectors plotted in Figs. 6(a)–6(d) can be obtained by comparing them with the electronic band structures in Figs. 2(a) and 2(b). The two lowest energy optical transitions around $E_m \approx 1$ eV shown in Figs. 6(a) correspond to the $\pi \rightarrow \pi^*$ transitions of graphite. Next, the optical transition around $E_m \approx 11$ eV may originally correspond to the $\pi \rightarrow B_2$ or the $\pi \rightarrow A_2$ transition, since either choice is possible following Fig. 2(a). However, the $\pi \rightarrow A_2$ optical transition can be excluded by the selection

rule in Table II. At $E_m \approx 12$ eV, the intermediate state can be the A_1, or to the σ_1^* or σ_2^* bands (see Fig. 2). The nonzero value of the dipole vector corresponds to D_y for the $B_2 \rightarrow A_1$ transition, while the dipole vector becomes $\mathbf{D} = 0$ for $A_2 \rightarrow A_1$. The σ_1^* and σ_2^* bands as the intermediate states have A_1 and B_1 symmetries. The dipole vector for the $B_2 \rightarrow B_1$ and $A_2 \rightarrow B_1$ transitions are $\mathbf{D} = 0$ and D_y, respectively.

In Figs. 6(c) and 6(d), we show similar properties with those in Figs. 6(a) and 6(d), but now for the case of graphene. The direction of the dipole vector for the $\pi \rightarrow \pi^*$ transition at $E_m \approx 0$ eV along the Γ-K and K-M directions is D_x, which is consistent with the results from Grüneis *et al.* [23]. The $\pi \rightarrow B_2$ transition takes place at $E_m \approx 11$ eV and the dipole vector components for this transition are D_z and D_x, as shown in Figs. 6(c) and 6(d). In the case of the third and fourth lowest conduction bands in graphene, the band with A_1 symmetry (orange dots in Fig. 2 around the K point) and σ_1^* band with A_1 symmetry are both involved in the electron-photon excitation. The directions of the dipole vector for the $\pi \rightarrow A_1$ and $\pi \rightarrow \sigma_1^*$ transitions along the Γ-K and K-M directions are denoted by D_y and D_x, respectively.

To discuss the magnitude of the dipole vectors for a given transition, we project the wave function (plane wave) on the atomic wave functions [28,34]. The calculations show that the $\pi \rightarrow B_2$ transition has the largest dipole vector among the available transitions in Fig. 6 since the π and B_2 bands have the same p_z orbital shape. The $\pi \rightarrow \sigma_1^*$ transition has the smallest dipole vector because the σ_1^* band near the K point is formed by p_x and p_y orbitals which do not overlap with p_z. On the other hand, the $\pi \rightarrow \sigma_2^*$ and $\pi \rightarrow A_1$ transitions should also be taken into account because the σ_2^* and A_1 bands are formed by the s, p_x, and p_y orbitals. The dipole vectors for the $\pi \rightarrow \sigma_2^*$ and $\pi \rightarrow A_1$ transitions are however weaker than that for the $\pi \rightarrow B_2$ transition.

The electron-phonon matrix element calculation reveals that, although the TO and LA phonon modes have the same symmetry (A_1), the matrix element for the LA phonon mode near the K point is negligibly small. The insignificant electron-phonon interaction for the LA phonon mode near the K point physically originates from the direction of atomic displacements of the LA mode. In Figs. 7(a)–7(f), we show the calculated electron-phonon matrix elements as a function of the final state energy E_f in graphite and graphene. The dots and asterisks correspond to the coupling of the photoexcited electron with the ZA and TO phonon modes, respectively. The difference between graphene and graphite is physically related to the ZA phonon mode, which cannot (can) be observed in the ARPES spectra for graphene (graphite), because graphene does not have an interlayer electron-phonon interaction [35]. Besides, the value of the electron-phonon matrix element decreases with increasing E_f.

For the incident photon with $\hbar\omega \approx 11.1$ eV, photoexcited electrons in the B_2 band are scattered into the final states near the Γ point (see Fig. 2). In the case of graphite, the final states can be π^*, σ_1^*, or σ_2^*, as the intensity for the $\hbar\omega \approx 11.1$ eV arises from the coupling between the photoexcited electron and the TO phonon. From these facts, we can conclude that the ARPES intensity around 154 meV for $\hbar\omega \approx 11.1$ eV is due to the photoexcitation of an electron from the π band to the B_2 band which is then scattered by the TO phonon
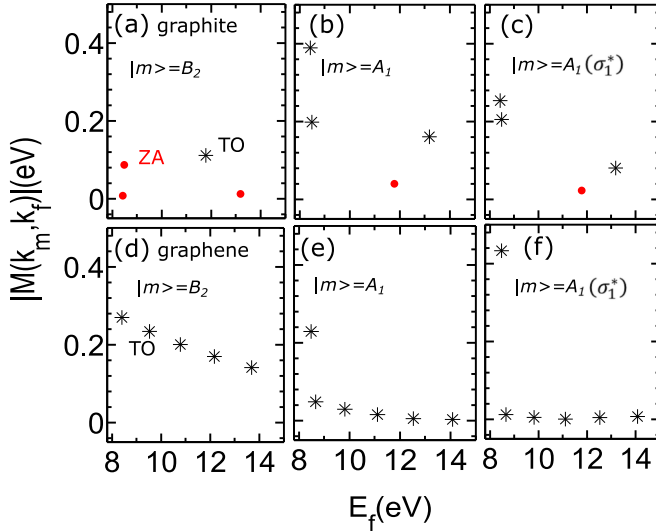
FIG. 7. The electron-phonon matrix elements for the scattering events from the intermediate states $|m\rangle$ with particular symmetries (B_2 and A_1) into some final states with different energies E_f. Panels (a)–(c) are for graphite, while panels (d)–(f) are for graphene. The dots and asterisks refer to the electron-phonon interaction for the ZA and TO phonon modes, respectively. Note that $|m\rangle$ in panels (b)–(c) and (e)–(f) have the same symmetries but originate from different bands. In particular, (c) and (f) are related to $|m\rangle$ of the σ_1^* band.

FIG. 8. Electron-phonon matrix elements for the ZA phonon mode of graphite for the transitions from an intermediate state $m\rangle$ having B_2 symmetry (the π^* band near the K point) into some different final states with energies E_f.

mode into a state near the Γ point. It should be noted that the discrepancy between the experimental and theoretical binding energy might come from the effect of the electron-electron correlation on the phonon dispersion [36], which is beyond the scope of this work. For $\hbar\omega \approx 13$ eV, the intermediate state can be associated with the A_1, σ_1^*, and or σ_2^* bands. In this case, both the ZA and TO phonon modes can be coupled with the photoexcited electron. However, the electron-phonon interaction for the ZA phonon mode is weaker than that for the TO phonon mode as discussed above. Thus, the ARPES intensity observed for $\hbar\omega \approx 12.5$ eV is assigned to the TO and ZA phonon modes.

B. Nonresonant indirect transition

Now we consider the case when the incident photon energy is $\hbar\omega \approx 6$ eV. The excitation process is the nonresonant indirect transition and the final state is the A_1 band, which is a nearly free-electron state. Let us again discuss the possibilities of the $A \to B \to D$ and $A \to C \to D$ transitions. If we assume that the virtual state comes from the closest real states of the electrons, the optical excitation in the second process ($\sigma_1, \sigma_2 \to A_1$) has a negligible intensity [37]. Furthermore, the optical transition along the high symmetry points on the Γ-A line (perpendicular to the Γ-K-M-Γ plane) for the second process also has a negligible intensity. Thus, the dominant mechanism should be the $A \to B \to D$ transition. As we mentioned before, although we find that the $A \to B \to D$ transition would also be more preferable for $\hbar\omega \approx 6$ eV, the physical argument for why this transition is dominant for $\hbar\omega \approx 6$ eV is different from that for $\hbar\omega \approx 11.1$ eV.
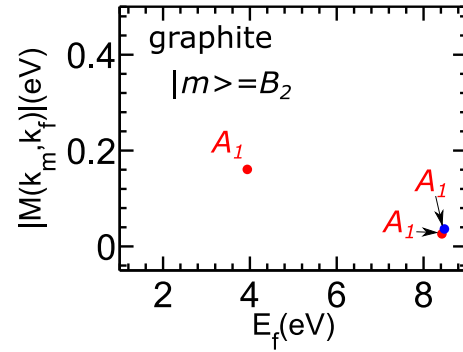
We can see that for the $A \to B \to D$ transition with $\hbar\omega \approx 6$ eV, the intermediate state is the B_2 band and the dominant dipole vector is D_z (see Fig. 6). Therefore, only the ZA phonon mode can be involved in this process (see Table II). The electron-phonon matrix element as a function of the final state is plotted in Fig. 8. It can be seen that there is a strong coupling between the π^* band and the A_1 band. The observation of the strong electron-phonon coupling between the π^* and A_1 bands was also reported with scanning tunneling spectroscopy by Zhang *et al.* and Wehling *et al.* [38,39]. We conclude that the ZA phonon mode corresponds to the ARPES signal at $E_b = 67$ meV if photons with $\hbar\omega \approx 6$ eV and p polarization are incident on the graphite surface.

When we look at the ARPES intensity for $\hbar\omega \approx 6$ eV and $\hbar\omega \approx 12.5$ eV in Fig. 5, there is a discrepancy between the experimental data of the ARPES intensity and the calculated results. The experimental ARPES intensity is higher than the calculated intensity for $\hbar\omega \approx 6$ eV, while the experimental ARPES intensity is much smaller than the calculated intensity for $\hbar\omega \approx 12.5$ eV. The origin of these discrepancies might be explained by the angle between the emission direction of the ejected photoelectron and the detector [7]. The direction of the detector is considered to be normal to the surface in the experiment [7,8] (see Fig. 4). In Table III, we show the shapes of the orbitals for the initial state $|i\rangle$, the intermediate state $|m\rangle$, the final state $|f\rangle$, the dipole vector direction $|O\rangle$, and the phonon polarization $|Ph\rangle$ for photon energies $\hbar\omega = 6$ eV, 11 eV, and 13 eV. Every initial state is in the π electron band, formed by the p_z orbital.

TABLE III. Phonon ($|Ph\rangle$) assignment for different photon energies ($\hbar\omega$). Columns for $|i\rangle$, $|m\rangle$, and $|f\rangle$ show the orbital shapes for initial, intermediate, and final states, respectively, while $|O\rangle$ denotes the direction of the dipole vector.

$\hbar\omega$(eV)	$|i\rangle$	$|O\rangle$	$|m\rangle$	$|Ph\rangle$	$|f\rangle$
6	p_z	D_z	p_z	ZA	s
11	p_z	D_z, D_y	p_z	TO	p_z
13	p_z	D_y	s, p_x, p_y	TO	s

For the $\hbar\omega \approx 6$ eV transition, the $|m\rangle$ state also has the p_z orbital character. The dipole vector becomes D_z and the out-of-plane phonon mode ZA also couples to the photoexcited electron. In this case, the final state $|f\rangle$ has an s orbital shape. Therefore, the ejected electron from this excitation process can be observed in the direction normal to the surface more strongly. For the $\hbar\omega \approx 11$ eV excitation, the $|m\rangle$ state also has a p_z shape and the dipole vector also becomes D_z. However, in this case, the electrons couple to the in-plane phonon mode TO and $|f\rangle$ has a p_z shape. As a result, the ejected electrons from this process also can be well observed in the direction normal to the surface. But we should note that the intensity of the observed electrons can decrease due to the coupling between the electron and the phonon mode. For the $\hbar\omega \approx 12.5$ eV, the intermediate state has s, p_x, p_y orbital shapes and the dipole vector is D_y and also the electron is coupled with the in-plane TO phonon mode, and in this case the final state has an s orbital shape. The ejected electrons from this process thus have a large dipole vector component parallel to the surface so that the possibility of the observation of the electrons from this process when the detector is normal to the surface will dramatically decrease.

C. Effects of s and p polarizations

Finally, we discuss the polarization dependence of the incident light for a single crystal of graphite. In Figs. 9(a) and 9(b), we plot the experimental and calculation data of graphite for s-polarized and for p-polarized light in the case of $\hbar\omega = 11$ eV. It can be seen that the ARPES intensity for p-polarized light is stronger than for s-polarized light for both experimental measurement and theoretical calculation. The physical reason for this behavior is that the z component of the vector potential (A_z) is stronger than the x component (A_x) for $\hbar\omega = 11$ eV and $\psi = 40°$, although the dipole vector components D_z and D_x have the same magnitude (see Fig. 6). Note that there is a small jump at $E_b = 0$ observed experimentally, originating from the phonon absorption in the indirect transition [7], that we did not consider in the calculations.

IV. SUMMARY

The indirect transition for the ARPES spectra in graphene and graphite have been investigated for different incident photon energies and light polarizations. We have compared the theoretical calculation of the indirect transition for the ARPES intensity of graphene and graphite with experimental measurements for HOPG and graphite. Our symmetry analysis shows that the ZA, TO, and LA phonon modes, which have even symmetry with respect to the mirror plane, $\sigma_v'(yz)$, can be involved in the indirect interband transition. Although the LA phonon mode has even symmetry with respect to the mirror plane, its phonon energy cannot be observed because it has a negligible electron-phonon interaction near the K point in the Brillouin zone. Thus, the ARPES spectra with binding energy $E_b = 154$ meV is assigned to the TO phonon modes of graphene and graphite when p-polarized photons with $\hbar\omega \approx 11$ eV are used. The relevant mechanism for the observation of the TO phonon mode is a resonant indirect transition. Meanwhile, for the incident photons with $\hbar\omega \approx 6$ eV, the ZA mode becomes dominant, being observable through a nonresonant indirect transition occurring in graphite for p-polarized light. Therefore, the phonon branches which can be observed by the ARPES measurement have been here assigned based on the detailed symmetry analysis and calculations, which were not available in the previous experiment [8]. Furthermore, the ARPES intensity of graphite for p-polarized light is stronger than for s-polarized light when the incident photon energy is $\hbar\omega \approx 11$ eV because the vector potential of the p-polarized light is expected to be stronger than that of s-polarized light.

By understanding the indirect transitions in the ARPES spectra of graphite and graphene, we expect that more detailed phonon dispersion relations might be observed in our future experiments. Besides, we believe that the validity of our methods should not be limited to graphene-based materials. We propose that the electron-phonon coupling for a large class of two-dimensional materials should also be observable by ARPES with indirect transitions.
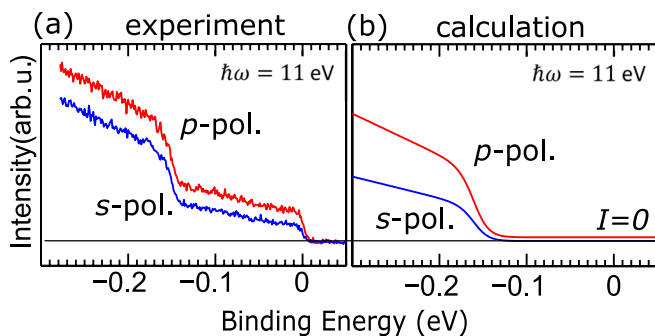
FIG. 9. (a) Experimental measurement and (b) theoretical calculation of the ARPES intensity as a function of the binding energy for a single crystal of graphite. The energy of the incident photon is $\hbar\omega = 11$ eV. The top and bottom curves correspond to the ARPES intensity for s-polarized and p-polarized light, respectively.

APPENDIX A: ELECTRON-PHONON INTERACTION

Let us define the equilibrium position of an atom $\sigma = A, B$ in the nth unit cell by $\mathbf{R}_\sigma^n$

$$\mathbf{R}_\sigma^n = \mathbf{R}_n + \mathbf{d}_\sigma \tag{A1}$$

where $\mathbf{R_n}$ and d_σ are, respectively, positions of the unit cell and the relative position of the σth atom in the unit cell.

The changes of the potential energy due to the lattice displacement are given by

$$\begin{aligned} H_{\mathrm{ep}} &= \sum_{n,\sigma} \left[V_n\big(\mathbf{r} - \mathbf{R}_\sigma^n + S_{n,\sigma}^\alpha(t)\big) - V_n\big(\mathbf{r} - \mathbf{R}_\sigma^n\big) \right] \\ &= \sum_{n,\sigma} S_{n,\sigma}^\alpha(t) \cdot \nabla_{\mathbf{R}_\sigma^n} V_n\big(\mathbf{r} - \mathbf{R}_\sigma^n\big), \end{aligned} \tag{A2}$$

in which $S_{n,\sigma}^\alpha(t)$ denotes the displacement vector of the atom and $\alpha = 1, \ldots, 6$ denotes the phonon mode, where

$$S_{n,\sigma}^\alpha(t) = A_\rho^\alpha(\mathbf{q}) e_\sigma^\alpha(\mathbf{q}) e^{i\mathbf{q}\cdot\mathbf{R}^n} e^{\pm i\omega^\alpha(\mathbf{q})t}, \tag{A3}$$

where A_ρ^α is the amplitude of the atomic vibration. The $\pm$ sign and ρ indices refer to whether a phonon is emitted ("$-$" and $\rho = E$) or absorbed ("$+$" and $\rho = A$). Here, $e^\alpha(\mathbf{q})$ is the unit vector of the lattice displacement vector, and $\omega(\mathbf{q})$ is the angular frequency of the phonon with a wave vector $\mathbf{q}$. The amplitude of the vibration A_ρ^α is given by

$$A_\rho^\alpha(\mathbf{q}) = \sqrt{\frac{2\hbar N_\rho^\alpha(\mathbf{q})}{m\omega^\alpha(\mathbf{q})N}} \tag{A4}$$

where N_ρ^α denotes the number of the phonons for the αth phonon mode and N is the number of atoms in the sample that contribute to the phonon; $m = 1.9927 \times 10^{-26}$ kg is the mass of a carbon atom. N_A^α and N_E^α are given by the Bose-Einstein distribution function as follows:

$$\begin{aligned} N_A^\alpha(q) &= \frac{1}{\exp\left(\frac{\hbar\omega^\alpha(\mathbf{q})}{k_B T}\right) - 1}, \\ N_E^\alpha(q) &= N_A^\alpha(q) + 1. \end{aligned} \tag{A5}$$

Here, we adopt the rigid-ion approximation where the potential V rigidly follows the motion of the ions [6,22]. Thus, the electron-phonon interaction Hamiltonian can be expressed by

$$H_{\mathrm{ep}} = -\sum_{n=0}^{N-1} \sum_{\sigma=A,B} \sum_{\alpha=1}^{6} A_\rho^\alpha(\mathbf{q}) S_{n,\sigma}^\alpha(t) \cdot \nabla_{\mathbf{r}} V_n\big(\mathbf{r} - \mathbf{R}_\sigma^{n,\alpha}\big), \tag{A6}$$

where we adopted the fact that $\nabla_r V_n = \nabla_R V_n$. Using perturbation theory, the nonzero matrix elements for this potential are given by

$$M_{\mathrm{ep}}^{v,v'}(\mathbf{k}_f, \mathbf{k}_i) = \langle \mathbf{k_f} | H_{\mathrm{ep}} | \mathbf{k_i} \rangle, \tag{A7}$$

where v and v' label the initial and final states.

To calculate the electron-phonon matrix elements, we expand the wave function of the initial states and final states in terms of plane waves,

$$\begin{aligned} \big| \mathbf{k}_i^v \big\rangle &= \frac{1}{\sqrt{V}} \sum_{\mathbf{G}} C_{\mathbf{G}}^{i,v}(\mathbf{k}_i) \exp\left(i(\mathbf{k}_i + \mathbf{G}) \cdot \mathbf{r}\right), \\ \big| \mathbf{k}_f^{v'} \big\rangle &= \frac{1}{\sqrt{V}} \sum_{\mathbf{G}'} C_{\mathbf{G}'}^{f,v'}(\mathbf{k}_f) \exp(i(\mathbf{k}_f + \mathbf{G}') \cdot \mathbf{r}), \end{aligned} \tag{A8}$$

where V is the volume of the sample, $\mathbf{G}$ represents the reciprocal lattice vector of graphene, and $C_{\mathbf{G}}^{i,v}(C_{\mathbf{G}}^{f,v'})$ are the plane-wave coefficients. Thus, the electron-phonon matrix elements are given by

$$\begin{aligned} M_{\mathrm{ep}}^{v,v'}(\mathbf{k}_f, \mathbf{k}_i) = &\frac{1}{V} \sum_{n=0}^{N-1} \sum_{\alpha=1}^{6} \sum_{\sigma=A,B} \sum_{\mathbf{G},\mathbf{G}'} C_{\mathbf{G}'}^{*f,v'}(\mathbf{k}_f) C_{\mathbf{G}}^{i,v}(\mathbf{k}_i) \\ &\times A_\rho^\alpha(\mathbf{q}) e^{i\mathbf{q}\cdot\mathbf{R}^n} e_\sigma^\alpha(\mathbf{q}) \cdot \mathbf{m}_D(\mathbf{k}_f, \mathbf{k}_i), \end{aligned} \tag{A9}$$

where $\mathbf{m}_D$ is expressed by

$$\mathbf{m}_D(\mathbf{k}_f, \mathbf{k}_i) = \int e^{i(\mathbf{k}_f - \mathbf{k}_i + \mathbf{G}' - \mathbf{G})\cdot\mathbf{r}} \nabla_{\mathbf{r}} V\big(\mathbf{r} - \mathbf{R}_\sigma^n\big) d\mathbf{r}. \tag{A10}$$

Then, by changing variables $\mathbf{r}' = \mathbf{r} - \mathbf{R}_\sigma^n$, and $d\mathbf{r}' = d\mathbf{r}$, $\mathbf{m}_D'(\mathbf{k}_f, \mathbf{k}_i)$ is expressed by

$$\mathbf{m}_D'(\mathbf{k}_f, \mathbf{k}_i) = \int e^{i(\mathbf{k}_f - \mathbf{k}_i + \mathbf{G}' - \mathbf{G})\cdot\mathbf{r}'} \nabla_{\mathbf{r}'} V(\mathbf{r}') d\mathbf{r}'. \tag{A11}$$

To obtain an explicit expression for the electron-phonon matrix element, we multiply the following unity relation into Eq. (A9):

$$1 = e^{i(\mathbf{k}_f - \mathbf{k}_i + \mathbf{G}' - \mathbf{G})\cdot\mathbf{R}_\sigma^n} e^{-i(\mathbf{k}_f + \mathbf{G}')\cdot\mathbf{R}_\sigma^n} e^{i(\mathbf{k}_i + \mathbf{G})\cdot\mathbf{R}_\sigma^n}. \tag{A12}$$

The electron-phonon matrix elements are given by

$$\begin{aligned} M_{\mathrm{ep}}^{v,v'}(\mathbf{k}_f, \mathbf{k}_i) = &\frac{1}{V} \sum_{n=0}^{N-1} \sum_{\alpha=1}^{6} \sum_{\sigma=A,B} \sum_{\mathbf{G},\mathbf{G}'} C_{\mathbf{G}'}^{*f,v'}(\mathbf{k}_f) C_{\mathbf{G}}^{i,v}(\mathbf{k}_i) \\ &\times A_\rho^\alpha(\mathbf{q}) e^{-i(\mathbf{k}_f - \mathbf{k}_i + \mathbf{G}' - \mathbf{G})\cdot\mathbf{R}_\sigma^n} e^{i\mathbf{q}\cdot\mathbf{R}^n} \\ &\times e_\sigma^\alpha(\mathbf{q}) \cdot \mathbf{m}_D'(\mathbf{k}_f, \mathbf{k}_i). \end{aligned} \tag{A13}$$

Using the fact that $\sum_{n=0}^{N-1} e^{-i(\mathbf{k}_f - \mathbf{k}_i - \mathbf{q} + \mathbf{G}' - \mathbf{G})\cdot\mathbf{R}^n} = \delta_{\mathbf{k}_f, \mathbf{k}_i + \mathbf{q}}$ in Eq. (A13) and using Eq. (A1), we get the following electron-phonon matrix element:

$$\begin{aligned} &M_{\mathrm{ep}}^{v,v'}(\mathbf{k}_f, \mathbf{k}_i) \\ &= \frac{1}{V} \sum_{\alpha=1}^{6} \sum_{\sigma=A,B} \sum_{\mathbf{G},\mathbf{G}'} C_{\mathbf{G}'}^{*f,v'}(\mathbf{k}_f) C_{\mathbf{G}}^{i,v}(\mathbf{k}_i) \\ &\quad \times A_\rho^\alpha(\mathbf{q}) e^{-i(\mathbf{k}_f - \mathbf{k}_i + \mathbf{G}' - \mathbf{G})\cdot\mathbf{d}_\sigma} \\ &\quad \times \delta_{\mathbf{k}_f, \mathbf{k}_i + \mathbf{q}} e_\sigma^\alpha(\mathbf{q}) \cdot \mathbf{m}_D'(\mathbf{k}_f, \mathbf{k}_i). \end{aligned} \tag{A14}$$

In order to obtain Eq. (A11), we expand an ion potential $V(\mathbf{r})$ of a free carbon atom, obtained by the *ab initio* method [40,41], into a sum of Gaussian basis functions as follows:

$$V(\mathbf{r}) = -\frac{1}{r} \sum_{p=1}^{4} v_p \exp\left(\frac{-\mathbf{r}^2}{2\tau_p^2}\right). \tag{A15}$$

TABLE IV. Coefficients v_p and τ_p for the ion potential $V(\mathbf{r})$ in Eq. (A15) [40,41]. The units of v_p are Hartree $\times$ a.u., and τ_p is in atomic units. (1 Hartree is 27.211 eV and 1 a.u. is 0.529177 Å.)

p	1	2	3	4
v_p	−2.13	−1.00	−2.00	−0.74
τ_p	0.25	0.04	1.00	2.80

The fitting parameters for the potential in Eq. (A15) are listed in Table IV.

Finally, putting Eq. (A15) into the Eq. (A11), we get $\mathbf{m}'_D(\mathbf{k_f},\mathbf{k_i})$ as follows

$$\mathbf{m}'_D(\mathbf{k_f},\mathbf{k_i}) = -i2\pi\sqrt{2\pi}\frac{\mathbf{Q}}{|\mathbf{Q}|}\sum_{p=1}^{4}v_p\tau_p\mathrm{Erfi}\left[\frac{|\mathbf{Q}|\tau_p}{\sqrt{2}}\right]$$

$$\times \exp\left[-\left(\frac{|\mathbf{Q}|\tau_p}{\sqrt{2}}\right)^2\right] \qquad (A16)$$

where $\mathbf{Q} = \mathbf{q} + \mathbf{G}' - \mathbf{G}$ and $\mathrm{Erfi}(z)$ is the imaginary error function and it is defined as

$$\mathrm{Erfi}(z) = -i\mathrm{Erf}(iz), \qquad (A17)$$

where $\mathrm{Erf}(z)$ is defined by

$$\mathrm{Erf}(z) = \frac{2}{\sqrt{\pi}}\int_0^z e^{-t^2}dt. \qquad (A18)$$

APPENDIX B: BASIC ARPES MECHANISM AND THE LATTICE SYMMETRY

ARPES is one of the spectroscopy methods to observe the electronic dispersion relations of the occupied bands of solids [42]. In the case of the direct transition, this process can be divided into three steps, the so-called three-step model: (1) photoexcitation of an electron inside the solid [see Fig. 10(a)], (2) travel of the photoelectron to the solid surface by an incident momentum [see Fig. 10(a)], and (3) emission of the photoelectron into the vacuum [see Fig. 10(c)].

The photoemission intensity as a function of the binding energy and momentum of the electron shows the electron dispersion relations of solids. The binding energies of the electron inside the sample and outside the sample, respectively, are determined by the energy conservation rules:

$$E_{\mathrm{kin,in}} = \hbar\omega - |E_b| \qquad (B1)$$

and

$$E_{\mathrm{kin,out}} = \hbar\omega - \phi - |E_b| \qquad (B2)$$

where $E_{\mathrm{kin,in}}$ and $E_{\mathrm{kin,out}}$ are the kinetic energy of electron inside and outside of the sample, respectively, $\hbar\omega$ is the photon energy, ϕ is the work function of the solid, and $|E_b|$ is the binding energy.

The momentum of the electron parallel to the surface of the solid is conserved during this process because the force is applied to the photoelectron only in the perpendicular direction to the surface [43], as shown in Fig. 10(c). Thus, the parallel momentum of the electron inside the sample is related to the
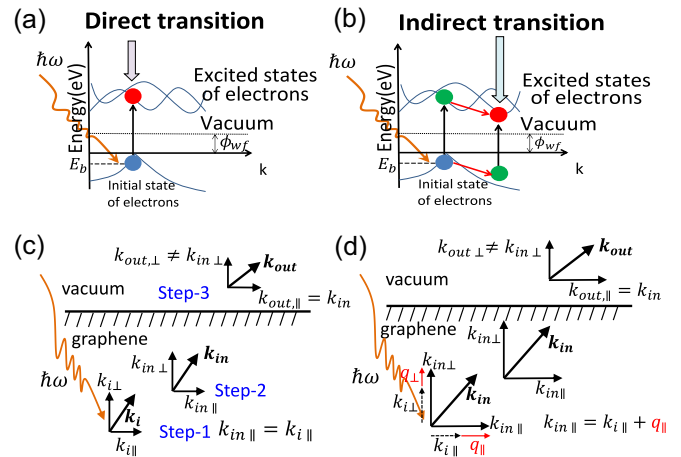

FIG. 10. Schematic representations of (a), (c) direct and (b), (d) indirect transitions. In the direct (indirect) transition, the momenta of the electron before and after the transition are the same (different). Panel (c) shows a photoemission process in the three-step model for the direct transition [43]. Panel (d) shows a photoemission process in the three-step model for the indirect transition. The difference between the direct and indirect transitions is on the first step, where the momentum of the phonon q is added to the momentum of the electron in the indirect transition.

parallel momentum of the electron outside of the sample as follows:

$$k_{\mathrm{out},\parallel} = k_{\mathrm{in},\parallel}. \qquad (B3)$$

In the case of the indirect transition [see Fig. 10(b)], although the three-step model is still appropriate, the first step of energy and momentum conservation has an additional term [see Fig. 10(d)], which comes from the momentum of the phonon. The energy conservation outside of the sample is written as follows:

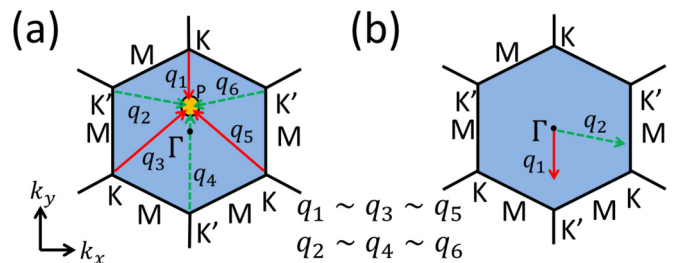$$E_{\mathrm{kin,in}} = \hbar\omega - \phi - |E_b + E_{b,q}| \qquad (B4)$$

FIG. 11. (a) Electrons are scattered from around the K or K' point into a $\mathbf{k}$ point, labeled P, shown in (a) as a yellow dot, along Γ-K by phonons. The phonon wave vectors which scatter electrons from K and K' into the observation point P are shown by red and green dot arrows, respectively. The phonon wave vector $\mathbf{q}_1,\mathbf{q}_3,\mathbf{q}_5$ and $\mathbf{q}_2,\mathbf{q}_4,\mathbf{q}_6$ indicate scattering from K and K' respectively. (b) Only two phonon momenta are inequivalent, whereas the phonon momenta $\mathbf{q}_3,\mathbf{q}_5$ and $\mathbf{q}_4,\mathbf{q}_6$ are folded back into the first Brillouin zone, $\mathbf{q}_1$ and $\mathbf{q}_2$, respectively, due to the lattice symmetry [7].

where $E_{b,q}$ expresses the binding energy of the electron after scattering and

$$k_{\text{out},\parallel} = k_{\text{in},\parallel} = k_{i,\parallel} + q_{\parallel} \qquad (B5)$$

where $q_{\parallel}$ is the additional momentum that the electron absorbs after the electron-phonon scattering.

In the case of graphene-based materials and similar materials, such as silicene and germanene, the highest binding energy of the electron is limited at the Fermi level ($E_b = 0$). Therefore, the energy conservation of the electron is reduced to

$$E_{\text{kin}} = \hbar\omega - \phi - |E_{b,q}|. \qquad (B6)$$

Then, resolving the energy of the electron after scattering becomes possible. Furthermore, in the indirect transition, since the observation of the electron is near the Γ point ($k_{\text{out},\parallel} = 0$), and the initial state of the electron is limited to be near the

$k_{\text{in},\parallel} = K$ point, the momentum conservation of the electron in this process is satisfied when $q_{\parallel} = K$.

Now, we consider that electrons are scattered by phonons from around the K or K' points into a certain **k** as shown by a yellow circle at the Γ-K line in Fig. 11(a). The phonon wave vectors which scatter electrons from the K and K' points into **k**, are shown by the red solid and green dot arrows, respectively. The phonon wave vectors $\mathbf{q}_1, \mathbf{q}_3, \mathbf{q}_5$ and $\mathbf{q}_2, \mathbf{q}_4, \mathbf{q}_6$ indicate scattering from the K and K' points, respectively. However, only two phonon momenta are inequivalent whereas the phonon momenta $\mathbf{q}_3, \mathbf{q}_5$ and $\mathbf{q}_4, \mathbf{q}_6$ are folded into the first Brillouin zone $\mathbf{q}_1$ and $\mathbf{q}_2$, respectively, due to the lattice symmetry [7], see Fig. 11(b). As a result, when the ARPES intensity along the Γ-K direction is investigated, the phonons Γ-K' and K-M-K' can also be observed. Similarly, when the ARPES intensity along the Γ-K' direction is investigated, the phonon along the Γ-K and K'-M-K directions can be observed. Thus, we can distinguish whether the electrons scatter from the K or K' points by observation of the Γ-K' or K-M-K' phonon dispersions, respectively.

[1] A. Damascelli, Z. Hussain, and Z. X. Shen, Rev. Mod. Phys. **75**, 473 (2003).

[2] A. Bostwick, T. Ohta, T. Seyller, K. Horn, and E. Rotenberg, Nat. Phys. **3**, 36 (2007).

[3] M. Calandra and F. Mauri, Phys. Rev. B **76**, 205411 (2007).

[4] W.-K. Tse and S. Das Sarma, Phys. Rev. Lett. **99**, 236802 (2007).

[5] G. D. Mahan, *Many-Particle Physics*, 3rd ed. (Springer, New York, 2000).

[6] G. Grimvall, *The Electron-Phonon Interaction in Metals* (North-Holland, Amsterdam, 1981).

[7] Y. Liu, L. Zhang, M. K. Brinkley, G. Bian, T. Miller, and T.-C. Chiang, Phys. Rev. Lett. **105**, 136804 (2010).

[8] S. Tanaka, M. Matsunami, and S. Kimura, Sci. Rep. **3**, 3031 (2013).

[9] P. Ayria, A. R. T. Nugraha, E. H. Hasdeo, T. R. Czank, S. I. Tanaka, and R. Saito, Phys. Rev. B **92**, 195148 (2015).

[10] C. Hamaguchi, *Basic Semiconductor Physics*, 2nd ed. (Springer-Verlag, Berlin, 2010).

[11] B. K. Ridley, *Quantum Processes in Semiconductors*, 5th ed. (Oxford University Press, New York, 2013).

[12] P. Giannozzi *et al.*, J. Phys.: Condens. Matter **21**, 395502 (2009).

[13] H. Luth, *Surface and Interfaces of Solid Materials* (Springer-Verlag, Berlin, 1995).

[14] M. Mucha-Kruczyński, O. Tsyplyatyev, A. Grishin, E. McCann, V. I. Fal'ko, A. Bostwick, and E. Rotenberg, Phys. Rev. B **77**, 195403 (2008).

[15] Y. Liu, G. Bian, T. Miller, and T.-C. Chiang, Phys. Rev. Lett. **107**, 166803 (2011).

[16] C. Hwang, C.-H. Park, D. A. Siegel, A. V. Fedorov, S. G. Louie, and A. Lanzara, Phys. Rev. B **84**, 125422 (2011).

[17] J. P. Perdew, K. Burke, and M. Ernzerhof, Phys. Rev. Lett. **77**, 3865 (1996).

[18] N. Mounet and N. Marzari, Phys. Rev. B **71**, 205214 (2005).

[19] S. Reich and C. Thomsen, Philos. Trans. R. Soc. London A **362**, 2271 (2004).

[20] M. S. Dresselhaus, G. Dresselhaus, P. C. Eklund, and D. D. L. Chung, Mater. Sci. Eng. **31**, 141 (1977).

[21] M. Mohr, J. Maultzsch, E. Dobardzic, S. Reich, I. Milosevic, M. Damnjanovic, A. Bosak, M. Krisch, and C. Thomsen, Phys. Rev. B **76**, 035439 (2007).

[22] O. J. Glembocki and F. H. Pollak, Phys. Rev. Lett. **48**, 413 (1982).

[23] A. Grüneis, R. Saito, Ge. G. Samsonidze, T. Kimura, M. A. Pimenta, A. Jorio, A. G. Souza Filho, G. Dresselhaus, and M. S. Dresselhaus, Phys. Rev. B **67**, 165402 (2003).

[24] S. Hufner, *Photoelectron Spectroscopy: Principles and Applications* (Springer-Verlag, Berlin, 1996).

[25] G. Giovannetti, P. A. Khomyakov, G. Brocks, V. M. Karpan, J. van den Brink, and P. J. Kelly, Phys. Rev. Lett. **101**, 026803 (2008).

[26] L. M. Malard, M. H. D. Guimarães, D. L. Mafra, M. S. C. Mazzoni, and A. Jorio, Phys. Rev. B **79**, 125426 (2009).

[27] E. Kogan and V. U. Nazarov, Phys. Rev. B **85**, 115418 (2012).

[28] E. Kogan, V. U. Nazarov, V. M. Silkin, and M. Kaveh, Phys. Rev. B **89**, 165430 (2014).

[29] M. S. Dresselhaus, G. Dresselhaus, and A. Jorio, *Group Theory: Application to the Physics of Condensed Matter* (Springer-Verlag, Berlin, 2008).

[30] S. K. Mahatha and K. S. R. Menon, Surf. Sci. **606**, 1705 (2012).

[31] S. Reich, C. Thomsen, and J. Maultzsch, *Carbon Nanotubes: Basic Concepts and Physical Properties* (Wiley-VCH, Weinheim, 2004).

[32] J. Maultzsch, S. Reich, C. Thomsen, H. Requardt, and P. Ordejón, Phys. Rev. Lett. **92**, 075501 (2004).

[33] F. de Juan, A. Politano, G. Chiarello, and H. A. Fertig, Carbon **85**, 225 (2015).

[34] V. M. Silkin, J. Zhao, F. Guinea, E. V. Chulkov, P. M. Echenique, and H. Petek, Phys. Rev. B **80**, 121408 (2009).

[35] K. Sato, J. S. Park, R. Saito, C. Cong, T. Yu, C. H. Lui, T. F. Heinz, G. Dresselhaus, and M. S. Dresselhaus, Phys. Rev. B **84**, 035419 (2011).

[36] M. Lazzeri, C. Attaccalite, L. Wirtz, and F. Mauri, Phys. Rev. B **78**, 081406 (2008).

[37] A. G. Marinopoulos, L. Reining, A. Rubio, and V. Olevano, Phys. Rev. B **69**, 245419 (2004).

[38] Y. Zhang, V. W. Brar, F. Wang, C. Girit, Y. Yayon, M. Panlasigui, A. Zettl, and M. F. Crommie, Nat. Phys. **4**, 627 (2008).

[39] T. O. Wehling, I. Grigorenko, A. I. Lichtenstein, and A. V. Balatsky, Phys. Rev. Lett. **101**, 216803 (2008).

[40] J. Jiang, R. Saito, A. Grüneis, G. Dresselhaus, and M. S. Dresselhaus, Chem. Phys. Lett. **392**, 383 (2004).

[41] J. Jiang, R. Saito, Ge. G. Samsonidze, S. G. Chou, A. Jorio, G. Dresselhaus, and M. S. Dresselhaus, Phys. Rev. B **72**, 235408 (2005).

[42] A. Damascelli, Phys. Scr. **T109**, 61 (2004).

[43] S. Suga and A. Sekiyama, *Photoelectron Spectroscopy* (Springer-Verlag, Berlin, 2014).